Originally published as:

Imaging the Dead Sea Transform with scattered seismic waves

N. Maercklin,[1]* C. Haberland,[1,2] T. Ryberg,[1] M. Weber,[1,2] Y. Bartov[3]
and the DESERT Group

[1] *GeoForschungsZentrum Potsdam, Telegrafenberg,* D-14473 *Potsdam, Germany*
[2] *University of Potsdam, PO Box 601553,* D-14476 *Potsdam, Germany*
[3] *Ministry of National Infrastructures, 216 Jaffa St. Box 36148, Jerusalem* 91360, *Israel*

SUMMARY

With controlled seismic sources and specifically designed receiver arrays, we image a subvertical boundary between two lithological blocks at the Arava Fault (AF) in the Middle East. The AF is the main strike-slip fault of the Dead Sea Transform (DST) in the segment between the Dead Sea and the Red Sea. Our imaging (migration) method is based on array beamforming and coherence analysis of *P* to *P* scattered seismic phases. We use a 1-D background velocity model and the direct *P* arrival as a reference phase. Careful resolution testing is necessary, because the target volume is irregularly sampled by rays. A spread function describing energy dispersion at localized point scatterers and synthetic calculations for large planar structures provides estimates of the resolution of the images. We resolve a 7 km long steeply dipping reflector offset roughly 1 km from the surface trace of the AF. The reflector can be imaged from about 1 km down to 4 km depth. Previous and ongoing studies in this region have shown a strong contrast across the fault: low seismic velocities and electrical resistivities to the west and high velocities and resistivities to the east of it. We therefore suggest that the imaged reflector marks the contrast between young sedimentary fill in the west and Precambrian rocks in the east. If correct, the boundary between the two blocks is offset about 1 km east of the current surface trace of the AF.

Key words: Arava Fault, array seismology, beamforming, Dead Sea Transform, scattering, seismic migration.

GJI Seismology

1 INTRODUCTION

Seismic waves are subject to scattering at small inhomogeneities, where 'small' means scales significantly smaller than the dominant wavelength of the incident wave. The superposition of scattered seismic energy generated by statistical perturbation of elastic parameters is often used to model the seismic coda (e.g. Aki & Chouet 1975). A complementary approach is to model the subsurface as a layered medium. This approach forms the basis of many seismic processing and migration techniques as described in several textbooks such as Yilmaz (2001). Models based on single scattering from spatially localized scatterers fill the range between these two end-members (e.g. Nikolaev & Troitsky 1987; Lymnes & Lay 1989; Hedlin *et al.* 1994; Weber & Wicks 1996; Belfer *et al.* 1998; Rietbrock & Scherbaum 1999; Müller 2000) and form the basis of diffraction-stack or pre-stack Kirchhoff depth migration (e.g. Buske 1999; Yilmaz 2001).

Krüger *et al.* (1995, 1996) and Scherbaum *et al.* (1997) applied source and receiver array beamforming simultaneously (double

beamforming) to image inhomogeneities at the core–mantle boundary. Rietbrock & Scherbaum (1999) extended this technique to spherical wave fronts to locate sources of scattering and, among others, Belfer *et al.* (1998) and Müller (2000) worked with controlled-source data and acquisition geometries typical in exploration seismology.

It has been known for a long time that crustal fault planes can act as reflectors (e.g. Deacon 1943; Robinson 1945). More recently, Louie *et al.* (1988) and Hole *et al.* (2001) observed steeply dipping reflectors related to the San Andreas Fault Zone. Furthermore, near-vertical reflections are also known from other geological structures such as flanks of salt diapirs or steeply dipping sedimentary beds (e.g. Allenby 1962). However, in general, steeply dipping structures are not easily detected by conventional near-vertical seismic reflection surveys (e.g. Yilmaz 2001).

Here we present data from explosion-generated scattered waves at the Dead Sea Transform (DST) (Fig. 1). This experiment is part of the interdisciplinary research project DESERT (Dead Sea Rift Transect), which includes several geophysical and geological studies to resolve the structure and dynamics of the transform at different scales (DESERT Group 2000). The small-scale seismic structure was investigated by controlled-source 2-D and 3-D velocity
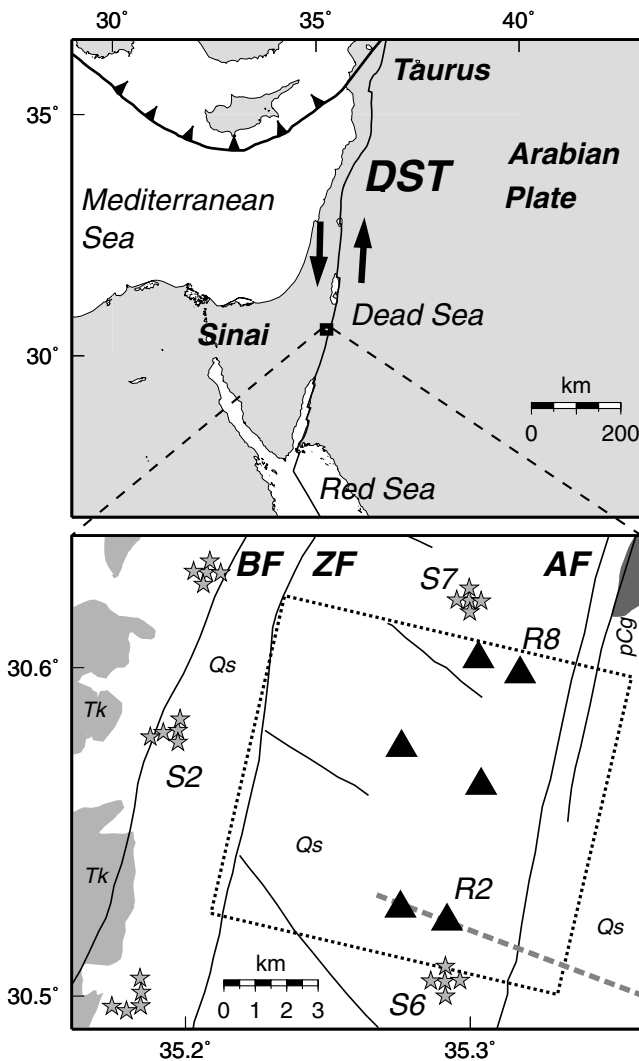
Figure 1. Top: Tectonic setting of the Dead Sea Transform (DST) in the Middle East. Bottom: Site map of the seismic imaging experiment at the Arava Fault (AF), the segment of the DST between the Dead Sea and the Red Sea. Stars indicate shot locations (S), triangles seismic receiver arrays (R), a dotted box outlines boundaries of Figs 5 and 6, and a dashed line marks coincident seismic and magnetotelluric profiles (Ritter *et al.* 2003). Fault trace locations are adopted from Frieslander (2000) and Rabb'a (1991) and surface geology from Bender (1975) (BF, Barak Fault; ZF, Zofar Fault; Qs, unconsolidated Quaternary sediments; Tk, lower Tertiary–Cretaceous limestones, chert and marl; pCg, Precambrian granites).

tomography, reflection seismics and the analysis of fault-zone guided waves (Maercklin *et al.* 2002; Haberland *et al.* 2003; DESERT Group 2004). Sources of seismic scattering in the area are expected to be related to the structure of faults. To image this structure down to a depth of about 4 km we designed and conducted an experiment with a combination of shots and receiver arrays followed by a special migration technique.

2 GEOLOGICAL SETTING

The Dead Sea Transform (DST) is a prominent shear zone in the Middle East. It separates the Arabian Plate from the Sinai microplate and stretches from the Red Sea Rift in the south to the Taurus–Zagros collision zone in the north (Fig. 1). Formed in the Miocene around

17 Ma and related to the break-up of the Afro-Arabian continent, the DST accommodates the sinistral movement between the two plates (Freund *et al.* 1970; Garfunkel 1981). The total amount of displacement is ∼105 km, and the present relative motion between the African and Arabian plate is between 3 and 4 mm yr^{-1} (Klinger *et al.* 2000).

Between Red Sea and Dead Sea the Arava Fault (AF) constitutes the major branch of the DST and takes up most of the slip (Garfunkel 1981; Atallah 1992). In the study area (Fig. 1) the AF strikes at N12°E. Scarps, pressure ridges, small rhomb grabens and water holes outline the fault trace in the field (Klinger *et al.* 2000). In the northern part of the study area, Rabb'a (1991) inferred a second fault strand striking parallel to the AF, 1 km to the east of it. More to the east, the subsurface is segmented into several blocks by additional faults, and outcrops of Precambrian granites occur (Fig. 1). *En echelon* tectonic basins of varying depth, filled with clastic sediments, characterize the region west of the AF (Bartov *et al.* 1998). The Zofar Fault (ZF) forms the western margin of such a basin. Contrary to the AF, the movement at the ZF is predominantly normal with the downthrown block to the east. Within the basin sediments are layered subhorizontally or dipping slightly to the north, seismic *P* velocity shows only minor lateral variation (e.g. Maercklin *et al.* 2002) and the Precambrian basement is reached at a depth of 2–2.5 km (Ritter *et al.* 2003; DESERT Group 2004). The area is in part covered by young alluvial sediments and aeolian sands.

3 EXPERIMENT DESIGN AND OBSERVATIONS

During a controlled-source seismic experiment we deployed six seismic receiver arrays, each with 10 stations (Fig. 2), and five clusters of five shots each west of the surface trace of the AF. Distances from receiver arrays to the AF were in the range 1.5 to 5 km, and shots were located 1 to 10 km away from the array centres (Fig. 1, Table 1). The main target area of this experiment was the AF and its vicinity.

Receiver arrays are often used in passive seismological experiments, since they allow direct measurement of wave slowness and azimuth by forming array beams (e.g. Harjes & Henger 1973; Krüger *et al.* 1995). Each receiver array in this study had an aperture of about 800 m, consisted of ten 1 Hz three-component seismometers and the sampling rate was 5 ms (DESERT Group 2000). The
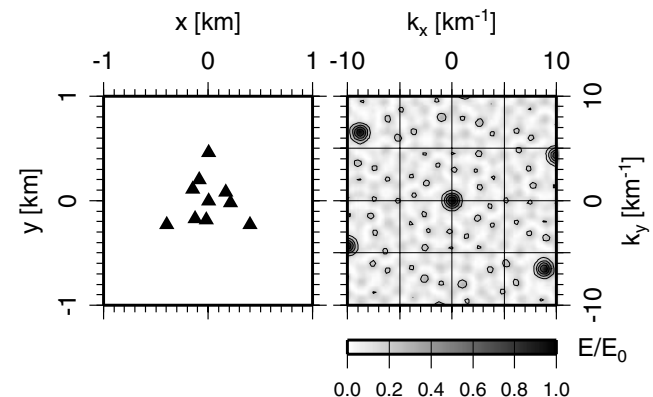

Figure 2. Receiver array geometry of the 10 seismometers (left) and corresponding array transfer function (right). Horizontal coordinates are labelled *x*, *y* and wavenumber components k_x, k_y respectively. Note the isotropic resolution and the sharp main lobe of the array transfer function.

Table 1. Centroid coordinates of shot (S) and receiver arrays (R), and the local coordinate system origin used in this study.

ID	Latitude (°N)	Longitude (°E)	Altitude (m)
S1	30.499228	35.181154	34.4
S2	30.580318	35.194480	−13.3
S3	30.628882	35.207422	−45.7
S6	30.504604	35.291148	132.0
S7	30.620416	35.299591	−46.4
R1	30.526856	35.275491	91.2
R2	30.522775	35.291830	79.3
R4	30.575595	35.275717	26.0
R5	30.564170	35.303674	55.5
R7	30.602576	35.302740	−21.6
R8	30.598020	35.317453	−18.9
Origin	30.495884	35.307839	0.0

aperture was set to pre-experimental spatial coherence measurements. Seismometers were arranged in a pattern suggested by Haubrich (1968) to achieve the best omnidirectional resolution. Fig. 2 shows this pattern for a single array together with its corresponding array transfer function. The array transfer function gives the amount by which energy of seismic phases with slowness different from the array steering vector is reduced by beamforming (Harjes & Henger 1973; Krüger *et al.* 1995; Buttkus 2000). Good resolution is indicated by a narrow main maximum and low power elsewhere. Spatial aliasing is apparent in repeating sidelobes, i.e. subsidiary maxima (Fig. 2, right).

Shots were arranged in groups of five individual shots each (Fig. 1) to enable array processing techniques such as (double) beamforming (Krüger *et al.* 1995, 1996) to take place on the source side. At each shot point 45 kg (S6, S7) or 60 kg (S1, S2, S3) of chemical explosives were detonated in boreholes 20 m deep. Because of land access restrictions, shot arrays could not be designed uniformly.

All shots excited strong direct *P* waves with a high signal-to-noise ratio. At later times, we observe near-surface reverberations of the direct *P* wave, which partially obscure scattered phases and thus must be removed prior to the analysis of scattering. *S* waves are not clearly visible, but from a local earthquake we estimated an average v_P/v_S ratio of about 1.83. Observed frequencies of the first *P* onset and its coda range from about 4 Hz to more than 20 Hz with an average peak around 8–10 Hz. Waveforms of direct first *P* arrivals are very coherent for a single shot recorded by all stations of an individual receiver array. On the other hand, signals generated at the same shot array often look quite different due to the local geology at a respective shot location. Therefore, we use the individual shots separately and apply array techniques only to receiver arrays.

4 IMAGING METHOD AND DATA PROCESSING

The sketch in Fig. 3 illustrates the basic idea behind the imaging concept. Seismic energy excited by a single shot is recorded by an array of receivers. The first arrival is the direct *P* wave, and a second arrival labelled *PxP* is due to scattering from a subsurface inhomogeneity. The traveltime of the *PxP* phase is given for each trace by the sum of the traveltimes of the two legs: from the source to the scatterer and from the scatterer to the corresponding receiver. Applying these moveout times as shifts to the initial recordings aligns the *PxP* phase. A stack of these aligned traces forms a *PxP* array beam and enhances this phase relative to *P*.

Generally, real data are contaminated by noise, and *PxP* has a small amplitude compared with *P*. Compared with a simple stack
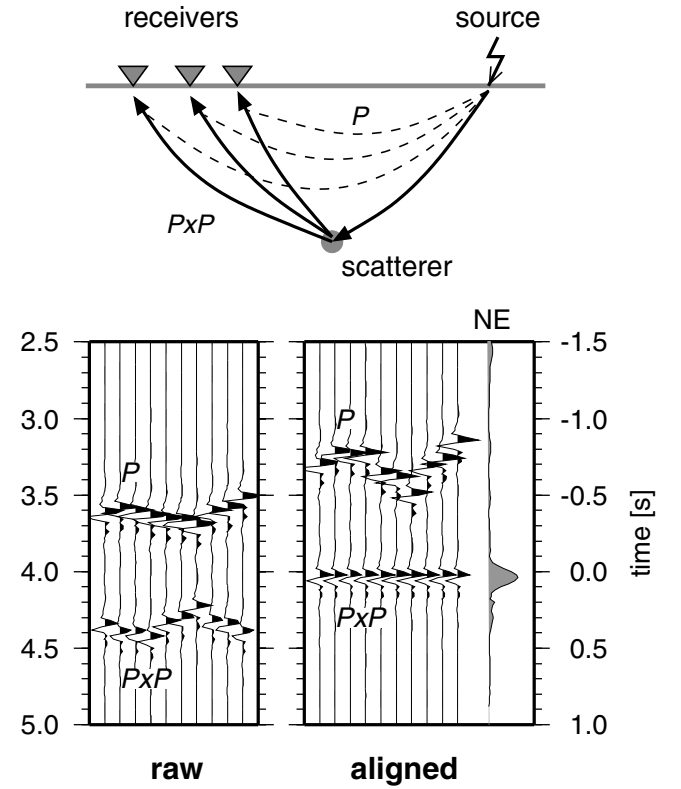
Figure 3. Top: Sketch showing ray paths for direct (*P*) and scattered waves (*PxP*). Bottom left: Raw synthetic receiver array recording for one shot and a single, omnidirectional point scatterer. Bottom right: The same panel with traces aligned according to the scatterer onsets of *PxP*. The semblance trace, labelled NE, illustrates, that a high semblance value at the predicted *PxP* traveltime indicates correct alignment of *PxP*, i.e. correct localization of the scatterer.

of the traces, coherence measures are superior for the detection of such weak but coherent phases. We assume that such coherence of *PxP* within a receiver array is justified, because we observed very coherent direct *P* arrivals (Section 3) and because only a limited range of scattering angles is involved in the beamforming process. Like Rietbrock & Scherbaum (1999), we choose the semblance *NE* as a coherence measure (Neidell & Taner 1971; Yilmaz 2001) and calculate it in a time window centred around the predicted *PxP* traveltime, but other measures, e.g. a phase stack (Schimmel & Paulssen 1997), could also be used. The semblance is defined as

$$NE_k = \frac{1}{M} \frac{\sum_{j=k-N/2}^{k+N/2} \left(\sum_{i=1}^{M} f_{ij}\right)^2}{\sum_{j=k-N/2}^{k+N/2} \sum_{i=1}^{M} f_{ij}^2}, \tag{1}$$

where *M* aligned traces are analysed in a time window of *N* samples centred at sample *k*, and f_{ij} is the amplitude value on the *i*th trace at time sample *j*. In this study we use a 0.25 s Hanning-tapered time window, in which the semblance is calculated. A high semblance value observed for *PxP* indicates the presence of a scatterer at the corresponding location. Thus, a discrete scan through a subsurface volume results in an image of regions where strong sources of scattering are located. A stack of such individual semblance images obtained from all source–receiver array combinations of the data set (see also Section 5) provides the final image presented in Section 6.

The migration concept for scattered phases outlined above requires a velocity model of the subsurface. The standard plane wave

approach in earthquake array seismology uses a slowness and a horizontal azimuth for the receiver and the source array respectively. Since in our application possible scatterers may be situated close to source or receiver arrays, this plane-wave or far-field approach cannot be used. Furthermore, the known increase of velocity with depth, resulting in curved ray paths, has to be taken into account. Therefore, we derived a 1-D velocity model (Section 6) and from that build a traveltime table for all possible offsets and depths in the target volume using a finite-difference scheme (van Trier & Symes 1991). The finite-difference grid spacing is 10 m in the horizontal and vertical directions, and traveltimes for distances between grid nodes are interpolated. Our migration algorithm reads *PxP* traveltimes from this table, which decreases processing times compared with two-point ray tracing for each source–scatterer–receiver combination, because traveltimes of many subsurface points are needed simultaneously.

To improve the signal-to-noise level we analyse bandpass-filtered vertical-component data in the frequency range between 4 and 24 Hz. We apply static time shifts to all seismogram traces such that the observed direct *P* phase arrives at the time predicted by the 1-D velocity model. Additionally, we calculate residual static corrections individually for each shot–receiver array combination using a technique adopted from Rothman (1986) to refine static time-shifts. The procedure utilizes cross-correlations and simulated annealing to find the maximum stack power around the direct *P* phase. The approach of using a reference phase (direct *P*) is known as relative beamforming. With this relative beamforming we account for topography, near-surface low-velocity layers and smooth large-scale velocity perturbations in the target volume.

We remove the influence of the direct *P* phase with a difference filter by subtracting the *P* beam from each trace. This approach is referred to as beam correction by Hedlin *et al.* (1991) and was also applied similarly by Müller (2000) to common-offset gathers of marine seismic profiles. As we do not have an accurate *S*-velocity model, we could not remove the influence of possible *S*-wave energy in a similar fashion. Therefore, we restricted the analysis to the time window between the direct *P* and the estimated direct *S* traveltime.

As an example, Fig. 4 shows a shot gather of a single shot from array S6 recorded by receiver array R8 (Fig 1, Table 1). The direct *P* wave arrives at about 3.2 s in the panel on the left. The panel on the right contains the same traces after subtraction of *P* and aligned according to *PxP* for a scatterer at a depth of 2 km, ~1 km east of the surface trace of the AF. The relative maximum semblance value (*NE*) observed at the predicted traveltime (0.0 s in Fig. 4, right) indicates the possible presence of a scatterer at the corresponding subsurface position.

5 SYNTHETIC RESOLUTION TESTS

Careful resolution testing is necessary, because the target volume is irregularly sampled by rays, especially compared with industry-style 3-D surveys. Resolution and imaging quality for single scatterers depend on the accuracy of the velocity model, the spatial position of the scatterer relative to the source–receiver array spread, azimuthal coverage of observations, frequency content and time duration of coherent *PxP* energy, and on signal contamination with noise. Influences of near-surface low-velocity layers and smooth large-scale velocity perturbations in the imaged volume can be addressed by relative beamforming as mentioned above. An inaccurate velocity model would shift the apparent scatterer position to a different location, but would also reduce the observed coherence for *PxP*.
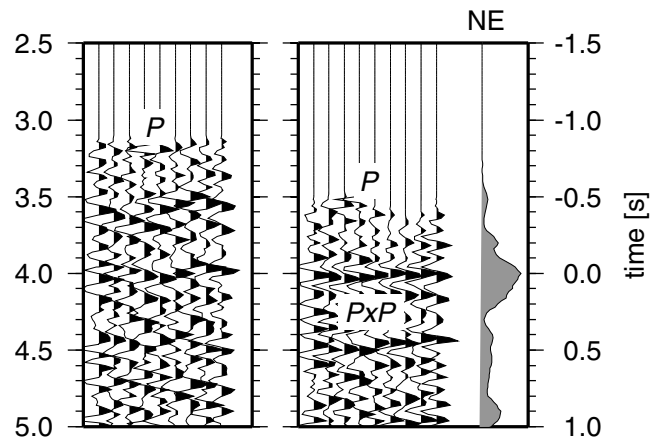

Figure 4. Vertical component shot gather of a single shot from array S6 recorded by receiver array R8 (Fig. 1), bandpass-filtered between 4 and 21 Hz and muted before *P*. Left: Unsorted traces after residual static corrections. Direct *P* arrives at about 3.2 s. Right: The same panel after subtraction of the direct *P* beam and with traces aligned according to *PxP* for a scatterer located at $x = 1.125$, $y = 8$, $z = 2$ km, ~1 km east of the AF (see also Fig. 6). Maximum semblance (trace labelled NE) is observed at the predicted *PxP* traveltime and indicates the presence of a scatterer (see also Fig. 3).

The imaging algorithm assumes that the scatterer is illuminated by a single arrival. In general, the incoming wave consists of a longer wave train, which results in smearing of energy outward from the actual location of the scatterer (e.g. Hedlin *et al.* 1994). Azimuthal resolution of a point scatterer by a single source and receiver array depends on array geometry. Energy is dispersed away from the true location of the scatterer to locations having the same *PxP* traveltime. For a uniform subsurface velocity model, this isochrone describes an ellipsoid with its foci at the source and at the centre of the receiver array (Hedlin *et al.* 1991, 1994; Müller 2000). However, a 2-D array design as used in this study reduces energy dispersion, whereas a straight receiver line would yield two maxima on the *PxP* isochrone, if the scatterer is not located vertically below this line.

Time averaging (as applied by Hedlin *et al.* 1994) or a longer analysis time window decreases radial resolution, whereas a long time window stabilizes the semblance calculation, provided that the window is not much longer than the duration of the coherent *PxP* phase. To increase radial resolution, and thus to suppress imaging artefacts, we stack semblance images obtained from different source–receiver array combinations. Stacking also suppresses the influence of spatially correlated noise, which would possibly be mapped into an apparent scatterer near the array (Hedlin *et al.* 1994). In the presence of spatially uncorrelated noise, beamforming combined with semblance analysis seems to be the optimum imaging technique for locating scatterers.

For a given subsurface velocity model and our acquisition geometry, imaging resolution and ambiguity can be assessed with synthetic calculations. To generate a synthetic data set, we calculate traveltimes for the direct *P* arrival and for *PxP* of a certain scatterer location, place spikes at these times on synthetic traces and weight spike amplitudes according to energy decay with increasing distance from the source. Then these traces are convolved with a synthetic wavelet, which we extract separately from each shot–receiver array combination of the real data. Thus, we also include effects of varying waveforms, as in reality, in our synthetic experiments. The wavelet-extraction algorithm averages the amplitude spectra, maps the average spectrum back into the time domain and finally

transforms the resulting zero-phase wavelet into its minimum-phase representation by twice-repeated Wiener inversion (e.g. see Buttkus 2000; Yilmaz 2001).

We conduct two sets of synthetic experiments for the given acquisition geometry and subsurface model. First, we image single, isolated point scatterers located at various positions in the subsurface volume and analyse energy dispersion. Second, we image planar structures consisting of several point scatterers. As with imaging of our real data (Section 6), we always assign the same local coordinate system (*x*-axis perpendicular to AF, *y*-axis parallel, origin given in Table 1) and divide the subsurface into blocks with an edge length of 125 m for beamforming and semblance analysis.

For the first set of experiments, we place single point scatterers at locations on a grid within the $12 \times 12 \times 4$ km box shown in Figs 1 and 5. The spacing of scatterers is 1 km in all directions. For each of the 845 scatterers we generate a synthetic data set as described above, containing only the response of the scatterer itself (*PxP* phase). Using our actual acquisition geometry, we image each scatterer individually. Variations in energy dispersion at all scatterer locations can be visualized by a spread function adopted from that defined by Michelini & McEvilly (1991) for model nodes in seismic tomography. At each assumed scatterer location j we use a spread function

$$S_j = \log \left(NE_j^{-1} \sum_{k=1}^{N} \frac{NE_k}{NE_j} D_{jk} \right), \tag{2}$$

in which k indicates image locations, NE_k the semblance at that point and D_{jk} the spatial distance between the image location and the assumed scatterer. The normalizing factor NE_j is the semblance for the assumed synthetic scatterer location and equals 1 in our test without pre-processing or random noise. The spread function is a relative measure of dispersion of energy away from a certain scatterer. Its distance term D_{jk} penalizes high semblance values mapped at locations far away from the true locations of the scatterers. Hence, high spread values indicate strong smearing of energy and thus lower resolution of point scatterers. Since it depends on subsurface parametrization, the spread function is not an absolute measure of imaging resolution. It only indicates variations of resolution for point scatterers in the imaged volume. Fig. 5 (left) shows spread values at several depth slices for our imaging parameters. The lowest resolution for point
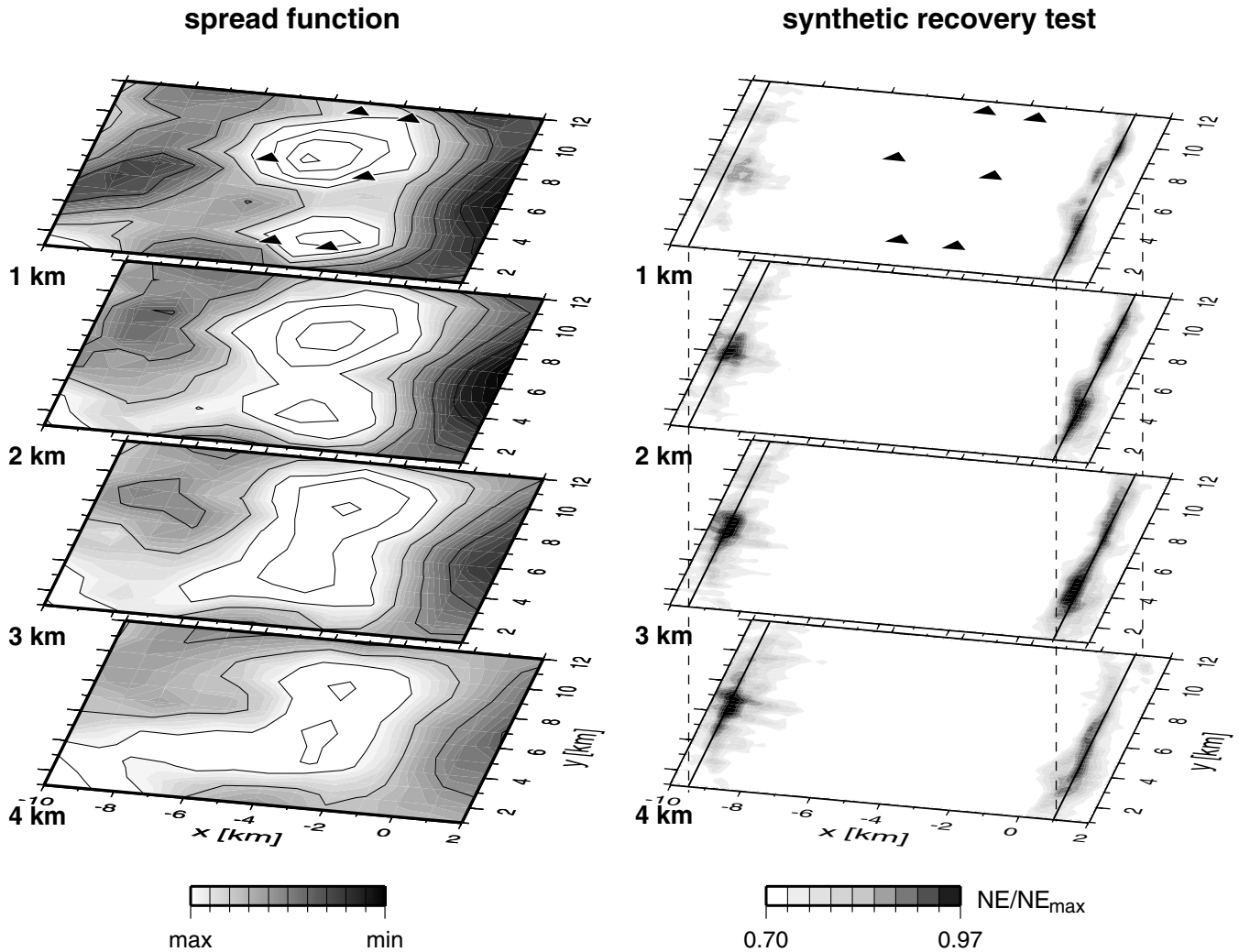

Figure 5. Left: First set of resolution tests: spread function values at four depth slices (units in km, box orientation as shown in Fig. 1). Dark areas correspond to low spread values (better resolution), and triangles in the top panel mark receiver array positions. Right: Second set of resolution tests: result of a synthetic recovery test for two vertical planes of scatterers at $x = -9.5$ km and $x = 1$ km, indicated by solid and dashed lines.

scatterers is obtained right beneath the receiver arrays. The lower resolution there is due to the small aperture of the receiver arrays (poor depth resolution) and the coarser spatial sampling of shots and receivers compared with conventional and more expensive 3-D acquisition geometries. The highest resolution is achieved in our main target area below the surface trace of the AF.

To study the resolution of subvertical zones of scattering related to faults, we conduct a second set of synthetic experiments. We generate a synthetic data set for two vertical planes of scatterers, in which scatterers are placed 0.5 km apart in horizontal and vertical directions down to a depth of 4 km. Based on indications in the real data, these planes are located under the ZF ($x = -9.5$ km) and 1 km east of the surface trace of the AF ($x = 1$ km). Additionally, we add random noise to all synthetic traces (20 per cent of the P amplitude) and apply the difference filter described in Section 3 to include its influence on the imaging result. Fig. 5 (right) shows the recovered image obtained with the same velocity model, acquisition geometry and subsurface parametrization as used for spread function calculation and for the real experiment. As expected from our acquisition geometry, scatterers at the ZF, located between several shots and the receiver arrays, can be detected only in a small region in the central part of the studied volume. In contrast to that, the plane of scatterers close to the AF, east of all shots and receivers, is imaged well from a depth of about 1 km to about 4 km along the segment between 3 and 10 km in the y-direction (parallel to the trace of the AF). Segments to the north and to the south are outside the optimum imaging aperture of the receiver array distribution. Analysis of subsets of the data have shown that the best imaging results are obtained by ray paths with grazing incidence, i.e. from S6 to R8 or from S7 to R2 (see Fig. 1).

6 IMAGING RESULTS AND DISCUSSION

To image the distribution of scatterers in the study area, we assign a local coordinate system with the origin given in Table 1. This system is rotated by 12° to have one axis roughly parallel to the surface trace of the AF (x-axis cross-fault, y-axis parallel). For beamforming and semblance analysis as described in Section 4, we assign a grid with a spacing of 125 m in all directions. We calculate the semblance in a 0.25 s Hanning-tapered time window, and accept data in the time window from direct P to expected direct S using a constant v_P/v_S of 1.83. The 1-D P velocity–depth function gradually increases from 2.3 km s^{-1} at the surface to 3.8 km s^{-1} at a depth of 1 km to 5.1 km s^{-1} at a depth of 4 km. Data processing includes static corrections and removal of the direct P phase (Section 4). The scanned subsurface volume exceeds that shown here to enable detection of possible artefacts at the boundary of the region reached in the allowed time window.

The final image of the scatterer distribution is a stack of all 150 individual, normalized images obtained from each shot–receiver array combination. Fig. 6 shows the scatterer distribution at four horizontal depth slices (left) and two vertical cross-sections (right) through the imaged volume. The semblance values in this final image are normalized to the maximum value. Absolute maxima are mostly below $NE \leq 0.5$.

We image a prominent subvertical zone of scattering (*reflector*) trending parallel about 1 km east of the surface trace of the AF and roughly coinciding with another fault strand in the northern part of the study area. In the WNW–ESE direction this structure is horizontally concentrated to about one to two subsurface blocks and is therefore just up to 250 m wide (Fig. 6, bottom right). From

SSW to NNE, we image the reflector between 3 and 10 km in the y-direction (Fig. 6, top right). Its further extension to the north and to the south remains unresolved as resolution degrades here (see Section 5 and Fig. 5, right). The resolved part of the reflector covers a depth range from more than 1 km to about 4 km. Above a depth of 1 km the image blurs, with one branch bending towards the surface trace of the AF. This feature is possibly a migration artefact in this very poorly resolved region and is therefore not included in our interpretation.

We interpret the imaged reflector at a depth of 1 to 4 km as a boundary between two different lithological blocks, which were most probably juxtaposed by displacement along the fault. The reflector coincides with a fault strand mapped east of the surface trace of the AF (Figs 1 and 6). The reflector position is also in agreement with an increase in the 3-D seismic P-velocity structure from west to east (Ryberg *et al.* 2001; Maercklin *et al.* 2002). Outcrops of Precambrian granites with high P velocities, mapped only east of the reflector (Fig. 1), support the interpretation that we imaged the boundary between the two lithological blocks. The western low-velocity block can be related to young sediments and basin fill (Section 2). Furthermore, there are indications for a correlation of the reflector position with subsurface changes of electrical resistivity revealed by magnetotelluric measurements (Ritter *et al.* 2001) in the central and northern part of the study area. South of the imaged reflector segment, the boundary between the two blocks seems to correlate with the AF as published by Ritter *et al.* (2003). Dashed lines in Figs 1 and 6 indicate the location of their coincident 2-D magnetotelluric and seismic tomography study. There, a conductive layer below a depth of 1 km terminates at or slightly east of the surface trace of the AF, and P velocities higher than 5 km s^{-1} are modelled about 1 km east of it, between a depth of 1 and 3 km. According to Ritter *et al.* (2003) the boundary acts as an impermeable barrier to fluid flow.

On the other hand, Haberland *et al.* (2003) found a narrow damage zone in the upper 300 m directly beneath the surface trace of the AF by modelling of seismic guided waves, and the western boundary of a shallow (∼100 m) electrically conductive layer in the east apparently also correlates with the surface trace of the AF (Ritter *et al.* 2001, 2003). Subhorizontal sedimentary reflections in the upper 1 km of the western basin (see Section 2) seem to terminate beneath the trace of the AF at about 10 km in the y-direction (seismic line VWJ-9, Natural Resources Authority of Jordan).

Surface geological mapping (Bender 1975; Rabb'a 1991) and shallow geophysical investigations delineate the current surface trace of the AF. At greater depths, below 1 km, the boundary between the two lithological blocks appears to be offset to the east. Recently, such an offset between the boundary of two blocks and the current fault trace at the surface has been suggested by Park & Roberts (2003) for the San Andreas Fault near Parkfield. At the AF, the relation between very shallow observations and deeper structures remains unresolved. Two possible models of the AF could explain our results. First, the AF could exhibit a rather complex shape, dipping to the east in the upper, unresolved 1 km and continuing subvertically 1 km east of its surface trace. Secondly, in our preferred model the AF consists of (at least) two branches spaced ∼1 km apart, where the eastern branch constitutes the main boundary between the different lithological blocks in the upper 4 km. As documented by the fault surface trace (scarps, pressure ridges, rhomb grabens, etc.), the western strand was probably active more recently. Surface geology with two parallel fault strands in the northern part of the study area (Fig. 1) supports the latter model. The total slip along the DST during the last 17 Myr may be distributed spatially and in
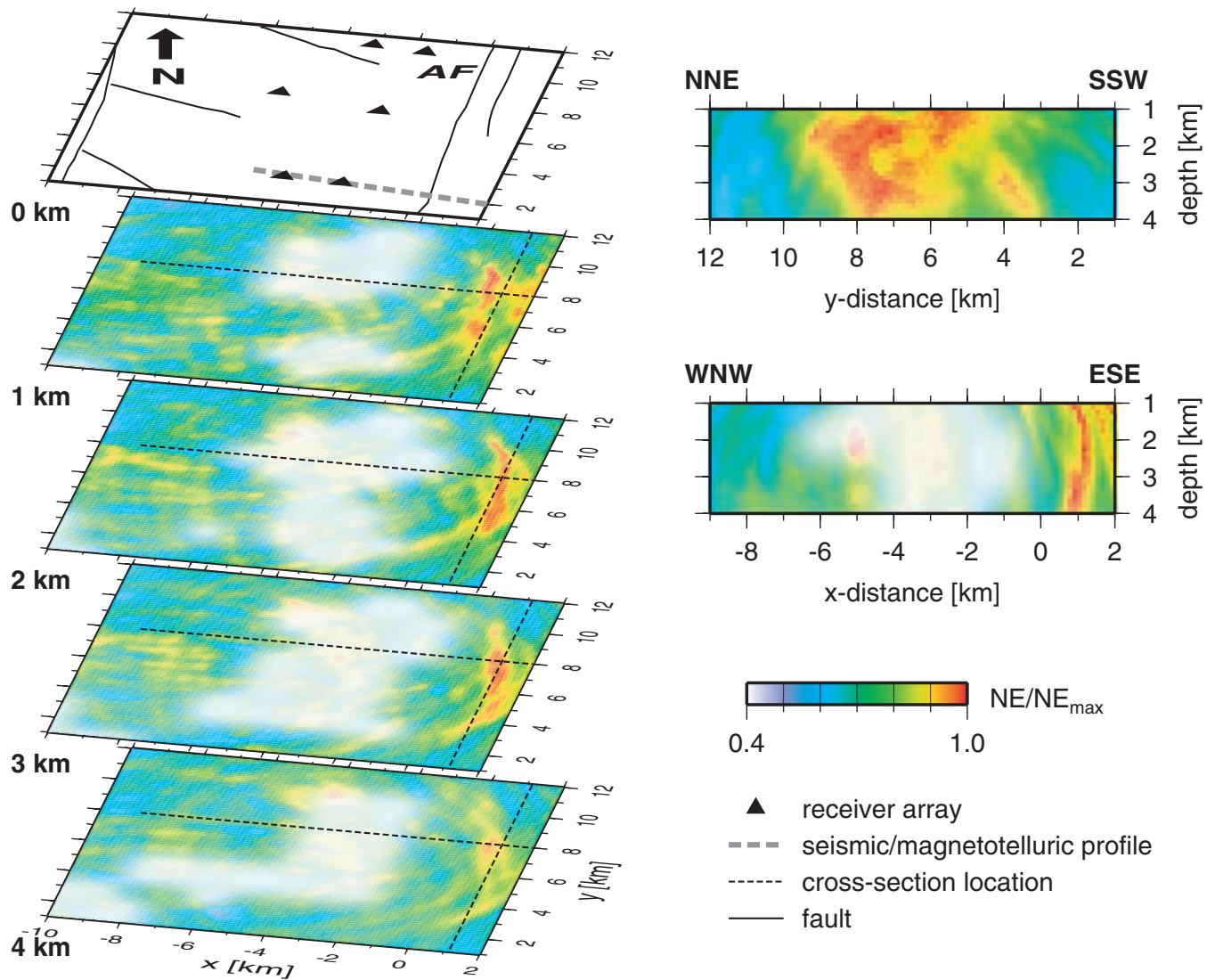
Figure 6. Colour-coded scatterer distribution in the vicinity of the Arava Fault (AF). Zones of strong scattering are in red. Areas with relatively high spread values (poor resolution) are whitened out. Left: The top panel shows fault traces, receiver arrays and a coincident seismic and magnetotelluric profile (Ritter *et al.* 2003) at the surface. Four horizontal depth slices show the distribution of scatterers (units in km, box orientation as in Fig. 1). Right: Two vertical cross-sections through the imaged volume at the two locations indicated by dashed lines in depth slices on the left (*x* = 1.125 km and *y* = 8 km respectively).

time over these (at least) two branches of the AF and possibly other faults such as the Quaira Fault further to the east, as also discussed previously by Haberland *et al.* (2003).

7 CONCLUSIONS

We successfully imaged a subvertical reflector along a 7 km long segment of the DST using controlled seismic sources and specifically designed receiver arrays. We imaged this reflector directly by analysing scattered seismic energy. This is in contrast to near-vertical reflection seismics, where vertical structures are generally inferred indirectly from offsets of more or less subhorizontal reflectors. In the case that the target region is roughly known *a priori*, the receiver array design used here can lead to 3-D images of subsurface structures with few seismic sources and stations (low-cost 3-D migration). Provided that source signals are similar enough, the migration algorithm can be used without modification for a double-beam imaging technique, and it is straightforward to implement *P* to *S* scattering.

The imaged reflector segment at a depth of between 1 and 4 km strikes parallel to the AF surface trace and is offset about 1 km to the east. It correlates with surface geological observations and the 3-D velocity structure derived independently from this study. The reflector marks the boundary between two lithological blocks juxtaposed at the DST and recently investigated by Ritter *et al.* (2003) south of our resolved structure. This boundary may be another strand of the AF, which is offset from its current surface trace, and the total slip of the DST may be distributed over these strands and possibly other faults. To extend the resolved region of this study, our acquisition layout has to be shifted north and south parallel to the AF, especially utilizing those shot–receiver combinations which lead to grazing-incidence ray paths. We propose to carry out similar experiments at other fault zones, where subvertical structures are expected.

ACKNOWLEDGMENTS

REFERENCES

Aki, K. & Chouet, B., 1975. Origin of coda waves: source, attenuation, and scattering effects, *J. geophys. Res.,* **80**(23), 3322–3341.

Allenby, R.J., 1962. The importance of reflected refractions in seismic interpreting, *Geophysics,* **27,** 966–980.

Atallah, M., 1992. Tectonic evolution of northern Wadi Araba, Jordan, *Tectonophysics,* **204,** 17–26.

Bartov, Y., Avni, Y., Calvo, R. & Frieslander, U., 1998. The Zofar Fault—a major intra-rift feature in the Arava rift valley, *Geol. Surv. Israel Curr. Res.,* **11,** 27–32.

Belfer, I., Bruner, I., Keydar, S., Kravtsov, A. & Landa, E., 1998. Detection of shallow objects using refracted and diffracted seismic waves., *J. appl. Geophys.,* **38,** 155–168.

Bender, F., 1975. *Geological Map of Jordan, 1:500000*, Government of Jordan and Geological Survey of the FRG. Hannover, Germany.

Buske, S., 1999. Three-dimensional pre-stack Kirchhoff migration of deep seismic reflection data, *Geophys. J. Int.,* **137**(1), 243–260.

Buttkus, B., 2000. *Spectral Analysis and Filter Theory in Applied Geophysics*, Springer, Heidelberg.

Cohen, J.K. & Stockwell, J.W., 2002. *CWP/SU: Seismic Unix Release 36: a free package for seismic research and processing*, Center for Wave Phenomena, Colorado School of Mines (http://www.cwp.mines.edu/cwpcodes/index.html).

Deacon, L.E., 1943. An analysis of abnormal reflexions, *Geophysics,* **8,** 3–8.

DESERT Group, 2000. Multinational geoscientific research kicks off in the Middle East, *EOS, Trans. Am. geophys. Un.,* **81**(50), 609, 616–617.

DESERT Group, 2004. The crustal structure of the Dead Sea Transform, *Geophys. J. Int.,* **156**(3), 655–681.

Freund, R., Garfunkel, Z., Zak, I., Goldberg, M., Weissbrod, T. & Derin, B., 1970. The shear along the Dead Sea rift, *Phil. Tran. R. Soc. Lond.,* **267,** 107–130.

Frieslander, U., 2000. The structure of the Dead Sea Transform emphasizing the Arava, using new geophysical data, *PhD thesis,* Hebrew University, Jerusalem (in Hebrew).

Garfunkel, Z., 1981. Internal structure of the Dead Sea leaky transform (rift) in relation to plate kinematics., *Tectonophysics,* **80,** 81–108.

Haberland, C. *et al.*, 2003. Modeling of seismic guided waves at the Dead Sea Transform, *J. geophys. Res.,* **108**(B7), doi:10.1029/2002JB002309.

Harjes, H.-P. & Henger, M., 1973. Array-Seismologie, *Z. Geophys.,* **39,** 865–905.

Haubrich, R.A., 1968. Array design, *Bull. seism. Soc. Am.,* **58,** 977–991.

Hedlin, M.A.H., Minster, J.B. & Orcutt, J.A., 1991. Beam-stack imaging using a small aperture array, *Geophys. Res. Lett.,* **18**(9), 1771–1774.

Hedlin, M.A.H., Minster, J.B. & Orcutt, J.A., 1994. Resolution of prominent crustal scatterers near the NORESS small-aperture array, *Geophys. J. Int.,* **119,** 101–115.

Hole, J.A., Catchings, R.D., St. Clair, K.C., Rymer, M.J., Okaya, D.A. & Carney, B.J., 2001. Steep-dip seismic imaging of the San Andreas fault near Parkfield, *Science,* **294,** 1513–1515.

Klinger, Y., Avouac, J.P., Karaki, N.A., Dorbath, L., Bourles, D. & Reyss, J.L., 2000. Slip rate on the Dead Sea transform fault in northern Araba valley, (Jordan), *Geophys. J. Int.,* **142**(3), 755–768.

Krüger, F., Weber, M., Scherbaum, F. & Schlittenhardt, J., 1995. Evidence for normal and inhomogeneous lowermost mantle and core-mantle boundary structure under the Arctic and northern Canada, *Geophys. J. Int.,* **122,** 637–657.

Krüger, F., Scherbaum, F., Weber, M. & Schlittenhardt, J., 1996. Analysis of asymmetric multipathing with a generalization of the double-beam method, *Bull. seism. Soc. Am.,* **86**(3), 737–749.

Louie, J.N., Clayton, R.W. & Le Bras, R.J., 1988. 3-D imaging of steeply dipping structure near the San Andreas fault, Parkfield, California, *Geophysics,* **53,** 176–185.

Lymnes, C.S. & Lay, T., 1989. Inversion of P coda for isotropic scatterers at the Yucca Flat test site, *Bull. seism. Soc. Am.,* **79,** 790–804.

Maercklin, N. *et al.,* 2002. Shallow structure of the Arava Fault (Dead Sea Transform) from seismic investigations, in, *EOS, Trans. Am. geophys. Un.,* **83**(Fall Meeting Supplement), S61A-1106.

Michelini, A. & McEvilly, T., 1991. Seismological studies at Parkfield. I. Simultaneous inversion for velocity structure and hypocenters using cubic B-splines parameterization, *Bull. seism. Soc. Am.,* **81,** 524–552.

Müller, C., 2000. On the nature of scattering from isolated perturbations in elastic media and the consequences for processing of seismic data, *PhD thesis,* Mathematisch-Naturwissenschaftliche Fakultät, Universität Kiel (http://e-diss.uni-kiel.de/diss_384/).

Neidell, N. & Taner, M.T., 1971. Semblance and other coherency measures for multichannel data, *Geophysics,* **36,** 482–497.

Nikolaev, A.V. & Troitsky, P.A., 1987. Lithospheric studies based on array analysis of P-coda and microseisms, *Tectonophysics,* **140,** 103–113.

Park, S.K. & Roberts, J.J., 2003. Conductivity structure of the San Andreas fault, Parkfield, revisited, *Geophys. Res. Lett.,* **30**(16), doi:10.1029/2003GL017689.

Rabb'a, I., 1991. *Geological Map: Al Qurayqira, 3051 II, 1:50000*, Natural Resources Authority, Geology Directorate, Amman, Jordan.

Rietbrock, A. & Scherbaum, F., 1999. Crustal scattering at the KTB from combined microearthquake and receiver analysis, *Geophys. J. Int.,* **136,** 57–67.

Ritter, O., Schmidt, J., Weckmann, U., Thoss, H., Abueladas, A. & Haak, V., 2001. A 3D magnetotelluric study of the Dead Sea Transform Fault in Jordan, in *EOS, Trans. Am. geophys. Un.,* **82**(Fall Meeting Supplement), S41A-0582.

Ritter, O., Ryberg, T., Weckmann, U., Hoffmann-Rothe, A., Abueladas, A., Garfunkel, Z., 2003. Geophysical images of the Dead Sea Transform in Jordan reveal an impermeable barrier for fluid flow, *Geophys. Res. Lett.,* **30**(14), doi:10.1029/2003GL017541.

Robinson, W.B., 1945. Refraction waves reflected from a fault zone, *Geophysics,* **10,** 535–545.

Rothman, D.H., 1986. Automatic estimation of large residual statics corrections., *Geophysics,* **51,** 332–346.

Ryberg, T., Garfunkel, Z., Qabbani, I. & El-Kelani, R., 2001. Shallow, high-resolution velocity structure across the Dead Sea transform fault, Dead Sea rift valley, from Vibroseis data—project DESERT 2000, in *EOS, Trans. Am. geophys. Un.,* **82**(Fall Meeting Supplement), S41A-0586.

Scherbaum, F., Krüger, F. & Weber, M., 1997. Double beam imaging: mapping lower mantle heterogeneities using combinations of source and receiver arrays., *J. geophys. Res.,* **102**(B1), 507–522.

Schimmel, M. & Paulssen, H., 1997. Noise reduction and detection of weak, coherent signals through phase-weighted stacks, *Geophys. J. Int.,* **130,** 497–505.

van Trier, J. & Symes, W.W., 1991. Upwind finite-difference calculation of traveltimes, *Geophysics,* **56**(6), 812–821.

Weber, M. & Wicks, C.W., 1996. Reflections from a distant subduction zone, *Geophys. Res. Lett.,* **23**(12), 1453–1456.

Wessel, P. & Smith, W.H.F., 1998. New, improved version of Generic Mapping Tools released., *EOS, Trans. Am. geophys. Un.,* **76,** 579.

Yilmaz, Ö., 2001. *Seismic Data Analysis*, Investigations in Geophysics Vol. 10, Society of Exploration Geophysicists, Tulsa, OK.